Helical Morphologies of Thermotropic Liquid-Crystalline Chiral Schiff-Based Rod−Coil Amphiphiles

Tz-Feng Lin,[†] Rong-Ming Ho,*,[†] Chien-Hung Sung,[‡] and Chain-Shu Hsu*,[‡]

Department of Chemical Engineering, National Tsing-Hua University, Hsinchu 30013, Taiwan, Republic of China, and Department of Applied Chemistry, National Chiao Tung University, Hsinchu 30050, Taiwan, Republic of China

A series of Schiff-based rod−coil molecules possessing thermotropic liquid-crystalline (LC) character have been prepared whereas a sugar-based moiety was introduced to the chain end of the molecules so as to create chiral amphiphiles for self-assembly. The self-assembly of the chiral Schiff-based rod−coil amphiphiles gave rise to a variety of specific LC textures. A banded morphology under polarized light microscopy (PLM) can be observed; the appearance of the banded texture is strongly dependent upon the length of hydrophobic tail that determines the twisting power of self-assembled hierarchical superstructures with helical sense. As a result, the banded spherulites are identified as quaternary helical morphology with a collection of the tertiary chiral structures (i.e., helical twists) so as to give regular extinction in PLM attributed to zero-birefringence effect. Consistent with the observation of helical morphologies, the occurrence of chiral smectic C (SmC*) phase can only be found in samples with enough alkoxyl chain length, suggesting the existence of strong correlation for morphological evolution from molecular level to macroscopic object with the formation of SmC*. A hypothetic model about the bilayer structure within the SmC* structure is thus given to elucidate the morphological evolution. Consequently, the self-assembly of the chiral amphiphiles with thermotropic LC character represents the mechanism for the chirality transfer in different length scales.

Introduction

Self-assembly of molecules toward hierarchical super-structures without human intervention plays an important role in nature that constructs structural elements from microscopic to macroscopic level.[1,2] Helicity, the most fascinating building blocks of fundamental interests in biology arises from primary structure (i.e., chiral molecular configuration) to secondary structure (helical chain conformation), tertiary structure (hierarchical superstructure with helical sense), and quaternary structure (chiral phase). The best known example of helical morphology has been found in chiral liquid crystals. Based on molecular consideration, three kinds of major helical liquid-crystalline phases: cholesteric, twisted grain boundary smectic A phase (TGBA), and chiral smectic C* (SmC*) have been observed.[3−5]

Chiral amphiphiles provide a rich library of chiral building blocks, which are also biocompatible, which makes them attractive candidates for being used successfully in the design of self-assembly chemistry.[6−9] One of the most famous families is sugar-based amphiphiles in which the sugar entity exhibits inherent chiral effect in the self-assembly. Glycolipids are basic constituents of biological membranes, and a variety of dynamically changing morphologies in liquid-crystalline (fluid) state were observed.[10,11] The morphologies of glycolipids affected by the introduction of different hydrophilic or hydrophobic parts[12−14] and of unsaturation in the lipophilic moiety[15−20] have been thoughtfully studied.

* Authors to whom correspondence should be addressed. C.-S. Hsu: tel: 886-3-5712121-31523; fax: 886-3-5723764; e-mail: cshsu@mail.nctu.edu.tw. R.-M. Ho: tel: 886-3-5738349; fax: 886-3-5715408; e-mail: rmho@mx.nthu.edu.tw.
† National Tsing-Hua University.
‡ National Chiao Tung University.

(1) Lehn, J.-M. *Science* **2002**, *295*, 2400−2403.
(2) Whitesides, G. M.; Grzybowski, B. *Science* **2002**, *295*, 2418−2421.
(3) Goodby, J. W. *Handbook of Liquid Crystals*; Demus, D., Goodby, J. W., Gray, G. W., Spiess, H.-W., Vill, V., Eds.; Wiley-VCH: Weinheim, 1998.
(4) Kitzerow, H.-S.; Bahr, C. *Chirality in Liquid Crystals*; Kitzerow, H.-S., Bahr, C., Eds.; Springer: New York, 2001.
(5) Goodby, J. W.; Waugh, M. A.; Stein, S. M.; Chin, E.; Pindak, R.; Patel, J. S. *J. Am. Chem. Soc.* **1989**, *111*, 8119−8125.

(6) Fuhrhop, J. H.; Helfrich, W. *Chem. Rev.* **1993**, *93*, 1565−1582.
(7) Spector, M. S.; Price, R. R.; Schnur, J. M. *Adv. Mater.* **1999**, *11*, 337−340.
(8) Spector, M. S.; Selinger, J. V.; Singh, A.; Rodriguez, J. M.; Price, R. R.; Schnur, J. M. *Langmuir* **1998**, *14*, 3493−3500.
(9) Estroff, L. A.; Hamilton, A. D. *Chem. Rev.* **2004**, *104*, 1201−1217.
(10) Laurent, N.; Lafon, D.; Dumoulin, F.; Boullanger, P.; Mackenzie, G.; Kouwer, P. H. J.; Goodby, J. W. *J. Am. Chem. Soc.* **2003**, *125*, 15499−15506.
(11) Gronwald, O.; Shinkai, S. *Chem. Eur. J.* **2001**, *7*, 4328−4334.
(12) Van Doren, H. A.; Smits, E.; Pestman, J. M.; Engberts, J. B. F. N.; Kellogg, R. M. *Chem. Soc. Rev.* **2000**, *29*, 183−199.
(13) Jung, J. H.; Yoshida, K.; Shimizu, T. *Langmuir* **2002**, *18*, 8724−8727.
(14) Zhou, Y.; Ji, Q.; Masuda, M.; Kamiya, S.; Shimizu, T. *Chem. Mater.* **2006**, *18*, 403−406.
(15) John, G.; Masuda, M.; Okada, Y.; Yase, K.; Shimizu, T. *Adv. Mater.* **2001**, *13*, 715−718.
(16) John, G.; Jung, J. H.; Minamikawa, H.; Yoshida, K.; Shimizu, T. *Chem. Eur. J.* **2002**, *8*, 5495−5500.
(17) Shimizu, T.; Jung, J. H.; John, G.; Yoshida, K. *J. Am. Chem. Soc.* **2002**, *124*, 10674−10675.
(18) Masuda, M.; Vill, V.; Shimizu, T. *J. Am. Chem. Soc.* **2002**, *122*, 12327−12333.
(19) Boyd, B. J.; Drummond, C. J.; Krodkiewska, I.; Weerawardena, A.; Furlong, D. N.; Grieser, F. *Langmuir* **2001**, *17*, 6100−6107.
(20) Wang, G.; Cheuk, S.; Williams, K.; Sharma, V.; Dakessian, L.; Thorton, Z. *Carbohydr. Res.* **2006**, *341*, 705−716.

Membrane structures with twisted, helical, or cylindrical tubular morphologies that express the chirality of their molecular constituents at a supramolecular scale of nanometers or micrometers have been observed.

Several theories have been developed to discuss the chiral geometry of bilayer membranes from the structures of the chiral amphiphiles. Helfrich and Prost suggested that the bending energy of amphiphilic membranes is not always at the minimum when they are flat, due to the presence of chiral effect.[21] Furthermore, with consideration of the intrinsic bending force of curvature elasticity, tilted chiral lipid bilayers (TCLB) theory arising from cholesteric liquid-crystal concepts were thus proposed by Ou-Yang et al. on the basis of the bending and twisting of molecules, namely, tilted molecular packing.[22] A similar simulation conclusion was remarked by Selinger et al.[23] and Selinger and Schnur[24] while they accounted for continuum theory with respect to intrinsic bending force. Also, the helical pitch, size, and handedness of helical morphologies were predicted at the minimum free energy of particular structures.[25−27] Moreover, the kinetic transitions and mechanism in lipid bilayers, diacetylenic lipids, have been studied by Caffrey and co-workers. Various phases were determined experimentally in the diacetylenic lipids such as lamellar, ripple, tubule, cubic, and hexagonal phase that agree with theoretical prediction.[28,29]

In this study, a series of new sugar-based rod−coil amphiphiles has been synthesized to examine the chiral effect on the self-assembly of rod−coil molecules. In contrast to the self-assembly from solution,[30] thin film and bulk samples are used to simplify the complicated mechanism of self-assembled structures on various length scales. Recently, unique phase morphology has been found in hexa-*peri*-hexabenzocoronenes (HBC) with dove-tailed alkyl substituents at which banded spherulites were observed under polarized light microscopy (PLM).[31] It is also noted that banded spherulites are rarely found and discussed in small organic compounds. Surprisingly, banded spherulitic morphology can also be found in the self-assembly of chiral Schiff-based rod−coil amphiphiles by PLM. The formation of a unique banded morphology is mainly attributed to the chiral effect induced by the chiral sugar entity and amplified by the hydrophobic tail, leading to the formation of the SmC* structure so as to form twisted superstructures. We thus suggest that the morphology of banded spherulite is a quaternary chiral texture, which is regarded as a collection

Scheme 1. Chemical Structure
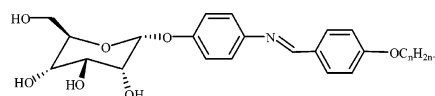
LC n (n = 7, 9, 11, and 13)

of tertiary chiral structures, namely, hierarchical superstructures with helical sense. Also, the size of the hydrophobic chain determines the twisting power for the self-assembled hierarchical superstructures with helical sense. As a result, the self-assembly chiral amphiphiles with thermotropic LC character represent the mechanism for the chirality transfer from molecular level to hierarchical superstructure, and finally macroscopic morphological texture. A model is also proposed to describe the twisting and bending origins in the banded spherulites of the chiral Schiff-based rod−coil amphiphiles. This may provide structural information on chiral material through molecular level to object exhibition in nature.

Experimental Section

Materials and Specimen Preparation. Scheme 1 indicates the general chemical structure of chiral Schiff-based rod−coil amphiphiles. The detailed synthetic routes combined with esterfication and Schiff condensation strategies have been published.[28] In general, the Schiff-based rod segment is served as mesogenic unit to drive the LC behavior in a self-assembly process whereas the alkoxyl chains are introduced to decrease the rigidity of the molecular structure. The number of alkoxyl chain lengths in the chiral Schiff-based rod−coil amphiphiles of this study is 7, 9, 11, and 13. They all possess the sugar entity as the chiral center in the head group, which is thus abbreviated as LC7, LC9, LC11, and LC13.

To examine the self-assembly mechanisms, samples cast from different concentrations were used to visualize the specific morphologies and also the self-assembled phases. Thin-film samples of the chiral Schiff-based rod−coil amphiphiles were solution-cast from a 0.05% (w/w) tetrahydrofuran solution on carbon-coated glass slide for TEM observations. By contrast, self-assembled morphologies of casting samples from a 2% (w/w) tetrahydrofuran solution were observed by PLM and field emission scanning electron microscopy (FE-SEM).

The cast thin films were heated on a heating stage above its highest endothermic transition temperature, held isothermally for 2 min, and then quenched to preset the annealing temperature for one to several hours. The annealing temperature was carefully selected to form high-ordered morphology where specific liquid-crystalline phase was formed first and then crystallization occurred. After crystallization, the thin films were removed from the glass slide, floated on the water surface, and recovered using copper grids for transmission electron microscopy (TEM) observations.

Characterization Techniques. Techniques such as differential scanning calorimeter (DSC), PLM, TEM, FE-SEM, and X-ray scattering were applied for structural characterization and morphological observations, whereas molecular simulation using Hyper-Chem 7 through the OPLS force field was also used for the understanding of molecular packing and calculating the layer-to-layer minimal energy geometry of chiral Schiff-based rod−coil amphiphiles.

The calorimetric measurements were carried out in Perkin-Elmer DSC 7 equipped with controlled cooling system in a flowing N_2 atmosphere. Temperature and heat flow scales at different scan rates

(21) Helfrich, W.; Prost, J. *Phys. Rev. A* **1988**, *38*, 3065−3068.
(22) Ou-Yang, Z.-C.; Liu, J.-X.; Yu-Zhang, X. *Geometric Methods in the Elastic Theory of Membranes in Liquid Crystal Phases*; World Scientific Publishing: Singapore, 1999.
(23) Selinger, J. V.; Wang, Z.-G.; Bruinsma, R. F.; Knobler, C. M. *Phys. Rev. Lett.* **1993**, *70*, 1139−1142.
(24) Selinger, J. V.; Schnur, J. M. *Phys. Rev. Lett.* **1993**, *71*, 4091−4094.
(25) Nandi, N.; Bagchi, B. *J. Am. Chem. Soc.* **1996**, *118*, 11208−11216.
(26) Nandi, N.; Bagchi, B. *J. Phys. Chem. A* **1997**, *101*, 1343−1351.
(27) Selinger, R. L. B.; Selinger, J. V.; Malanoski, A. P.; Schnur, J. M. *Phys. Rev. Let.* **2004**, *93*, 158103−1.-158103−4.
(28) Caffrey, M.; Hogan, J; Rudolph, A. S. *Biochemistry* **1991**, *30*, 2134−2146.
(29) Caffrey, M.; Cheng, A. *Curr. Opin. Struct. Biol.* **1995**, *5*, 548−555.
(30) Sung, C. H.; Kung, L. R.; Hsu, C. S.; Lin, T. Z.; Ho, R.-M. *Chem. Mater.* **2006**, *18*, 352−359.
(31) Pisula, W.; Kastler, M.; Wasserfallen, D.; Pakula, T.; Müllen, K. *J. Am. Chem. Soc.* **2004**, *126*, 8074−8075 and references therein.

(2.5, 5, 10, 20, and 40 °C/min) were calibrated with standard materials of cyclohexane and indium before experiments proceeded. Typically, the DSC sample weight was 2−3 mg to avoid a thermal gradient within the samples. The samples were heated above their isotropic melting temperatures for 2 min to eliminate possible effects of thermal history during synthetic routes and then cooled below the glass transition temperature at different scanning rates (2.5−40 °C/min). The consecutive heating was also performed at a rate that was equal to the prior cooling rate. When the DSC cooling curves were used to analyze the transition behavior, the on-set temperature of the transition in the high-temperature site was determined. When the heating curves were used, the on-set temperature was found from the low-temperature site.

Optical textures of the LC phases at different temperatures were observed with an Olympus BX-60 equipped with a hot stage by an INSTEC 200 central processor. It was carefully aligned before use and then was utilized to observe the thermal transitions and to analyze the optical textures. The hot stage was calibrated with standard materials within the precision of ±0.2 °C. The samples were thermally treated according to thermal analyses studies. The micrographs were held isothermally at the temperature where the transition was observed by DSC and X-ray scattering experiments.

A Siemens D5000 1.2 kW tube X-ray generator (Cu Kα radiation) with a diffractometer was used for wide-angle X-ray diffraction (WAXD) powder experiments. The scanning 2θ angle ranged between 1° and 35° with a step scanning of 0.05° for 3 s. The diffraction peak positions and widths observed from WAXD experiments were carefully calibrated with silicon crystals with known crystal size. A hot stage was set up on the diffractometer to study the structural changes during the phase transitions at constant cooling and heating rates. Nonisothermal experiment that was mounted on an aluminum sheet was performed at a rate of 5 °C/min. The background diffraction from an aluminum sheet itself was also collected and subtracted from the sample diffraction.

TEM experiments were carried out in JEOL JEM-1200CXII and JEOL 2010 at an accelerating voltage of 120 and 200 kV, respectively. Bright-field TEM images were obtained using the mass-thickness contrast from shadowing. Shadowing has proven useful in contrast enhancement by the addition of heavy metal in a vacuum evaporator. The samples were dropped on carbon film first and supported by a 400 mesh Cu grid that must fit into the specimen holder of the microscope, and then shadowed by Pt/Pb = 4/1 30° tilted to the surface. The electron diffraction (ED) experiments for the thin films were also carried out. Calibration of the ED spacing was done using TlCl in a *d* spacing range smaller than 0.384 nm, which is the largest spacing for TlCl. Spacing values larger than 0.384 nm were calibrated by doubling the *d* spacing of those diffractions based on their first-order diffractions.

Results and Discussion

Thermotropic LC Phase Behavior. To examine corresponding phase transition behavior for the synthesized materials, non-isothermal DSC measurements were performed at different scanning rates of 2.5, 5, 10, 20, and 40 °C/min. Figure 1 illustrates the thermograms of DSC cooling and heating scans for LC11. Significant thermal transitions at around 225, 100, and 50 °C in 10 °C/min cooling thermograms can be found. The change of cooling rate from 2.5 to 40 °C/min leads only to a 5 °C difference in the on-set temperature of highest transition (an exothermic response at around 225 °C), and the temperature discrepancy is mainly attributed to the effect of thermal lag during measurements as identified, suggesting that the transition is near equilib-
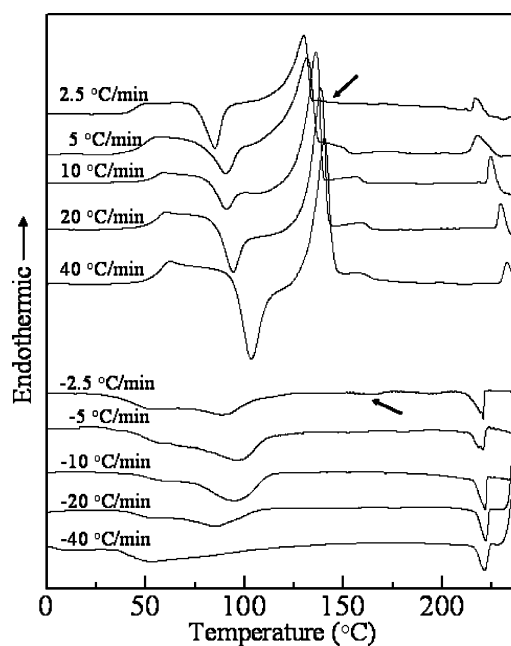

Figure 1. Thermograms of LC11 in different heating and cooling rates.

rium. By contrast, the intermediate transition (also an exothermic response) at around 100 °C exhibits a clear supercooling dependence (say ca. 15 °C different in the peak temperatures of 5 and 20 °C/min cooling thermograms), namely, a kinetic transition. For the lowest transition at around 50 °C, a step change on heat capacity can be identified, indicating the occurrence of glass transition. Upon heating, the glass transition can be further examined. Nevertheless, an exothermic response immediately followed by the glass transition can be identified, and then an endothermic response occurs. The on-set temperature of the endotherm is consistently higher than the on-set temperature of the exotherm at intermediate transition during cooling. Also, the discrepancy increases with the scanning rate. As a result, we suggest that the intermediate transitions involve crystallization and melting processes due to the occurrence of supercooling dependent process. It is also noted that there is a small endothermic peak during heating at ca. 150 °C as marked, and the corresponding exothermic response is barely identified during cooling where a small exothermic peak at ca. 160 °C can only be found in a low scanning (say 2.5 °C/min) thermogram. We speculate that this small enthalpy change is attributed to a liquid-crystalline transition (see next section in detail). In a high-temperature range, the on-set temperature of the endotherm corresponds well with the on-set temperature of the exotherm at highest transition in a cooling thermogram, regardless of the scanning rate, further confirming that the transition is a near equilibrium process, namely, a transition from a low-ordered liquid-crystalline phase to an isotropic melt. This reversible phase transition behavior on heating and cooling can be found in all of the samples studied, suggesting that the Schiff-based group in the synthesized compounds behaves as a mesogenic unit so as to lead the induction of thermotropic liquid-crystalline behavior with enantiotropic type. Table 1 summarizes the corresponding transitions of the chiral Schiff-based rod−coil amphiphiles during heating and cooling in different

Table 1. Thermal Analyses of Chiral Schiff-Based Rod−Coil Amphiphiles Studied

entry (scanning rate, °C/min)		thermal transitions (°C)	
		cooling	heating
LC7	2.5	I 193, SmA 88, K	K 124,[c] SmA 187, I
	5	I 192, SmA 85, K	K 125,[c] SmA 189, I
	10[e]	I 190, SmA 76, K	K 126,[c] SmA 190, I
	20	I 188, SmA 87,[b] K	K 133,[c] SmA 192, I
	40	I 188, SmA 75,[b] K	K 157,[c] SmA 192, I
LC9	2.5	I 207, SmA 175,[b] SmC* 109,[b] K 33, T_g	T_g 38, K 118,[c] SmC* 126,[c] SmA 198, I
	5	I 207, SmA 157,[b] SmC* 93,[b] K 34, T_g	T_g 40, K 126,[c] SmC* 139,[c] SmA 200, I
	10[e]	I 209, SmA 153,[b] SmC* 82,[b] K 35, T_g	T_g 42, K 127,[c] SmC* 145,[c] SmA 205, I
	20	I 211, SmA −, SmC* 82,[b] K 41, T_g	T_g 48, K 133,[c] SmC* 156,[c] SmA 212, I
	40	I 211, SmA −, SmC* 82,[b] K 42, T_g	T_g 52, K 135,[c] SmC* 158,[c] SmA 214, I
LC11[d]	2.5	I 219, SmA 161,[b] SmC* 93,[b] K 40, T_g	T_g 46, K 129,[c] SmC* 149,[x] SmA 211, I
	5	I 221, SmA 148,[b] SmC* 98,[b] K 40, T_g	T_g 46, K 133,[c] SmC* 151,[c] SmA 219, I
	10[e]	I 223, SmA −, SmC* 95,[b] K 52, T_g	T_g 55, K 136,[c] SmC* 157,[c] SmA 222, I
	20	I 224, SmA −, SmC* 85,[b] K 52, T_g	T_g 56, K 139,[c] SmC* 160,[c] SmA 228, I
	40	I 224, SmA −, SmC* −, K 52, T_g	T_g 57, K 140,[c] SmC* 160,[c] SmA 230, I
LC13	2.5	I 220, SmA 161,[b] SmC* 78,[b] K 4, T_g	T_g 46, K 129,[c] SmC* 146,[c] SmA 213, I
	5	I 222, SmA 163,[b] SmC* 80,[b] K 7, T_g	T_g 46, K 130,[c] SmC* 147,[c] SmA 219, I
	10[e]	I 225, SmA −, SmC* −, K 47, T_g	T_g 55, K 126,[c] SmC* 147,[c] SmA 224, I
	20	I 225, SmA −, SmC* −, K 49, T_g	T_g 56, K 128,[c] SmC* 147,[c] SmA 228, I
	40	I 225, SmA −, SmC* −, K 50, T_g	T_g 57, K 136,[c] SmC* 147,[c] SmA 230, I

[a] I = isotropic phase; SmA = smectic A phase; SmC* = chiral smectic C phase; K = crystalline phase; T_g = glass transition. Transition temperatures (°C) are determined by the on-set temperature of DSC profiles. [b] Temperatures (°C) determined by exothermic peak. [c] Temperatures (°C) determined by endothermic peak. [d] Thermograms of DSC cooling and heating scans are demonstrated in Figure 1. [e] Thermograms of DSC cooling and heating scans are demonstrated in Figure 2. [f] The enthalpies of the phase transitions from the DSC experiments are given in the Table S1 of Supporting Information.
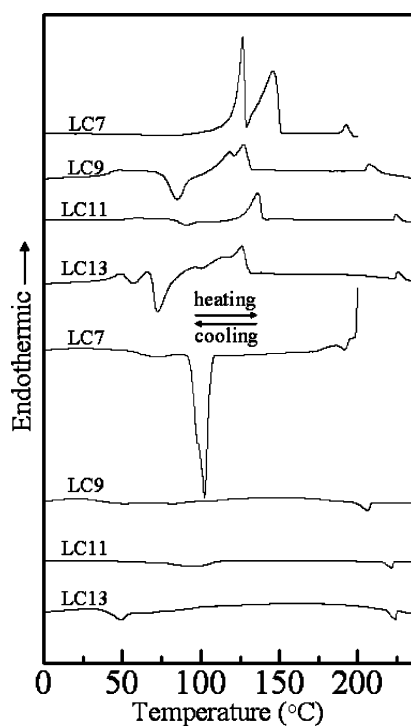

Figure 2. Thermograms of LC7, LC9, LC11, and LC13 in 10 °C/min cooling (lower part) and heating (upper part) scans.

scanning rates. To compare the phase transition behavior in all of the samples studied, similar equilibrium transition from a low-ordered liquid-crystalline to isotropic melt (i.e., the highest temperature transition) can be recognized. Figure 2 illustrates the DSC thermograms for various samples with different alkoxyl chain lengths. It is noted that the equilibrium transition temperature is dependent upon the alkoxyl chain length. The longer the alkoxyl chain length, the higher the equilibrium transition temperature. The entropy of the isotropic phase (S_i) decreases with the increase of the alkoxyl chain length attributed to the molecular weight effect, leading

to the increase of the free energies in the isotropic melt (G_i) (namely, the higher transition temperature).[32] For crystallization and melting processes (i.e., the intermediate transition), the increase of alkoxyl chain length will lower the crystallization rate as evidenced by the disappearance of exothermic peak in the intermediate temperature range of cooling thermograms. Consequently, complicated thermograms attributed to crystallization and melting during heating can be observed. In contrast to the small endothermic peak during heating after crystallization and melting, the heating thermogram of LC7 exhibits quite different thermal transitions at which significant endothermic responses can be found. To further investigate the thermal transitions of LC7, crystalline samples were prepared by cooling at 10 °C/min from melt (Figure S1 of Supporting Information) and then heating at different rates. There are always two major endothermic peaks even at different heating rates but the high melting peak temperature remains constant. By contrast, the corresponding enthalpy of the high melting peak exhibits a significant decrease with the increase of heating rate whereas the total enthalpy of these two melting peaks is nearly constant. This result indicates that the high melting peak is regarded as a reorganization phenomenon during heating. At a slow heating rate, the original crystals with the lower melting temperature reorganize to reach the crystals of the higher melting temperature (i.e., order perfection). The process of order perfection is strongly suppressed when the heating rate is too rapid to accomplish the reorganization. For the lowest transition region, T_g is absent in the DSC thermograms of LC7. We speculate that the crystallinity is too high for LC7 to experience glass transition. The discrepancies in thermal transitions of the chiral Schiff-based rod−coil amphiphiles might be responsible for the formation of various morphological textures with different alkoxyl
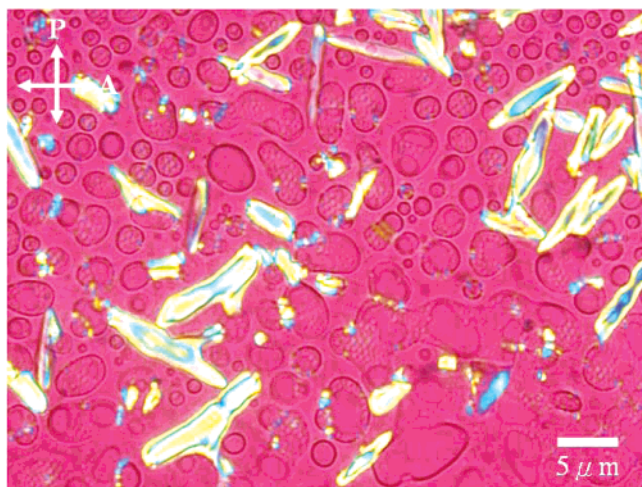
(32) Percec, V.; Keller, A. *Macromolecules* **1990**, *23*, 4347−4350.

5514 *Chem. Mater., Vol. 18, No. 23, 2006*

Lin et al.

Figure 3. PLM image of LC11 shows the SmA phase on the glass substrate at 200 °C from isotropic melt at 10 °C/min cooling.

chain lengths. Detailed phase transformation during cooling and heating will be further examined by PLM morphological observations and X-ray scattering experiments.

PLM Morphologies of Chiral Schiff-Based Rod−Coil Amphiphiles. To further examine the phase transformation of the chiral Schiff-based rod−coil amphiphiles, the self-assembled morphologies were observed during cooling and heating by using PLM from isotropic melt. Upon cooling, an interesting morphological transformation can be observed in all of the samples studied. First, a typical smectic A (SmA) texture can be identified once the temperature is below the highest transition temperature as illustrated in Figure 3. The SmA texture then disappears to become a transparent image without any specific textures. We speculate that the disappearance of birefringent texture is attributed to the ordering process from isotropic phase into low-ordered phase at which the optic axes of mesogenic units in SmA gradually align to the substrate normal of a glass slide during cooling. Homeotropic anchoring condition is achieved by the hydrophilic effect of the glass slide. The transparent morphology remains while the cooling process continues even reaching the intermediate temperature range. The phase difference in transparent SmA phase and isotropic melt under PLM can be simply distinguished by shearing at which SmA phase can be observed due to the induced homotropic orientation. In contrast to continuous cooling, a crystalline texture grown from the SmA phase can be found once the cooling is low enough to initiate crystallization process. Upon heating, the occurrence of the crystalline texture has been evidenced by PLM (for instance, at 100 °C in LC11) as illustrated in Figure 4a. The formation of crystalline morphology is consistent with the results of DSC heating thermograms. The preformed crystalline texture is then heated to the temperature above intermediate transition (140 °C for LC11) at which some strip pattern can be generated from the LC-like texture (see below for details) as shown in Figure 4b. Further increasing of the temperature, a SmA phase with homeotropic anchoring condition (i.e., a transparent image) can be found (150 °C for LC11), and the SmA phase remains until isotropic melting.

Delicate PLM observations are then performed to clarify the LC phase formed near intermediate transition. To examine the ordering processes involving crystallization growth and specific LC formation around the temperature range of intermediate transition, a series of isothermal crystallization studies are examined by DSC. As illustrated by LC11, the temperature of the maximum crystallization rate is found at 95 °C and the crystallization temperature range is found between 65 and 130 °C (Figure S2 of Supporting Information). Unique morphology (Figure 5c) is formed when the sample is isothermally treated at 125 °C from isotropic melt at which the formation of banded texture occurs, and then crystallization executes but not significant to overwrite the preformed liquid-crystalline texture. Note that the formation of a banded ring is strongly dependent on the alkoxyl chain length. In contrast to the formation of banded textures in LC9, LC11, and LC13 (Figures 5b−5d), typical crystalline spherulites in LC7 (Figure 5a) can be observed in the temperature range of intermediate transition. The absence of banded spherulites in LC7 might be attributed to the fast growth of crystallization to dominate the ordering process and/or the loss of specific LC phase with helical sense to induce the macroscopic chirality. Moreover, the remarkable banded spherulites gradually disappear and then transfer into SmA phase once the temperature is over the small endothermic peak during heating as marked in DSC (for instance, 150 °C in LC11). Similar phase transformation during heating can also be identified after the formation of SmA phase in all the samples studied. We speculate that the formation of banded spherulites is attributed to the molecular chirality in the liquid-crystalline materials at which chiral phase might be induced to create specific birefringence under PLM, namely, macromolecular helicity.[33−35] On the basis of molecular dispositions for the chiral Schiff-based rod−coil amphiphiles studied, a liquid-crystalline phase with helical sense, a SmC* phase, was thus proposed for the interpretation of the formed texture. Detailed structural analysis and morphology of the assumed SmC*, and the corresponding mechanism with respect to the formation of banded spherulites, will be discussed below.

Structures of Chiral Schiff-Based Rod−Coil Amphiphiles. To identify the structures of corresponding phase transitions, in particular, the assumed SmC* phase, X-ray experiments are performed on the bulk sample during cooling. As illustrated by the diffraction results of LC11, Figure 6 shows one-dimensional X-ray profiles of bulk samples at various temperatures. In the profiles at low-2θ-angle region, well-ordered diffraction peaks at characteristic ratios of 1:2:3:4 are found in all temperature ranges examined. It is also noted that the (002) reflection conceals in the scattering pattern, suggesting the well-defined structure has symmetrical layer-to-layer diffraction. For the highest transition (namely, high-temperature range), the layer-to-layer d-spacing in the SmA phase appears to be 5.20 nm determined from the primary scattering peak of X-ray

(33) Malthete, J; Jacques, J; Tinh, N. H.; Destrade, C. *Nature* **1982**, *298*, 46−48.

(34) Kajitani, T.; Okoshi, K.; Sakurai, S.-I.; Kumaki, J.; Yashima, E. *J. Am. Chem. Soc.* **2006**, *128*, 708−709.

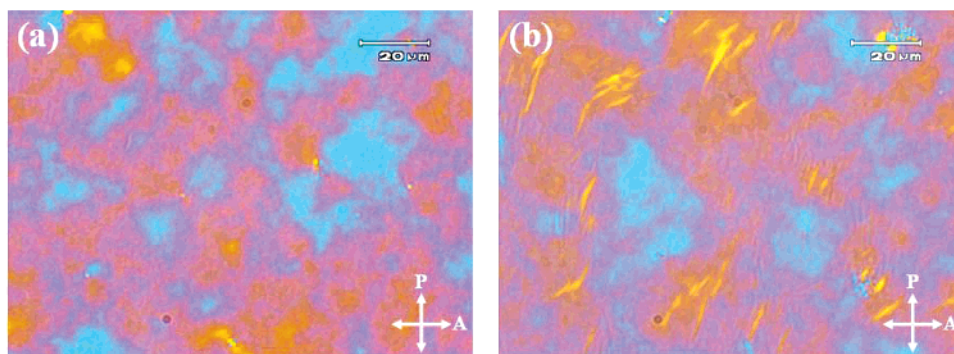(35) Goto, H.; Akagi, K. *Chem. Mater.* **2006,** *18*, 255−262.

Figure 4. PLM images of LC11 at (a) 100 °C and (b) 140 °C in heating procedure after continuous cooling from isotropic melt at 40 °C/min cooling.
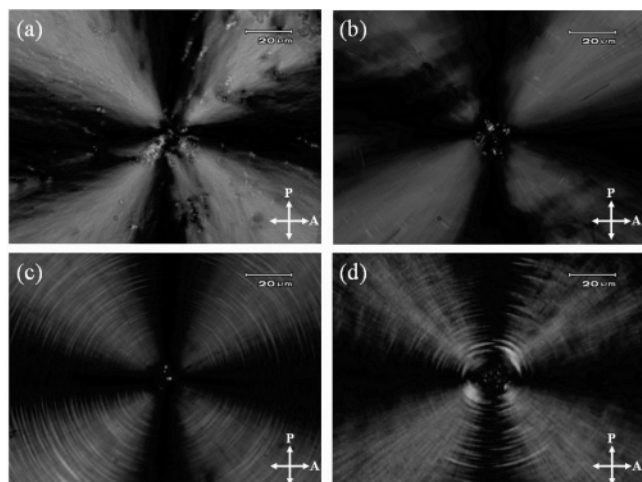

Figure 5. PLM morphologies of (a) LC7, (b) LC9, (c) LC11, and (d) LC13 at 125 °C from isotropic melt at 2.5 °C/min cooling (alkoxyl chain length dependence).
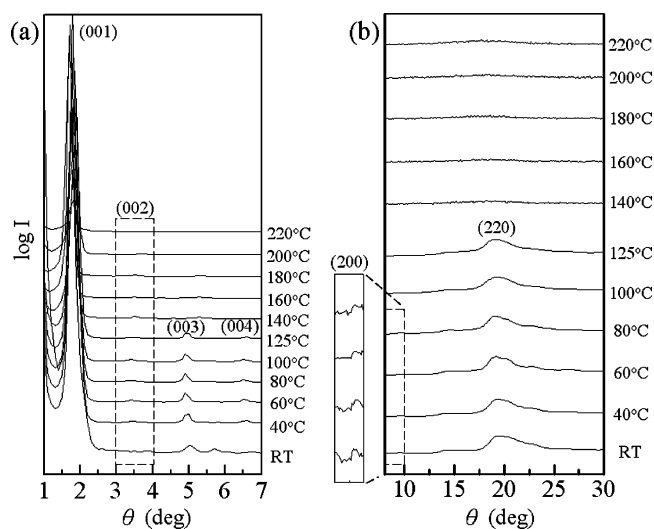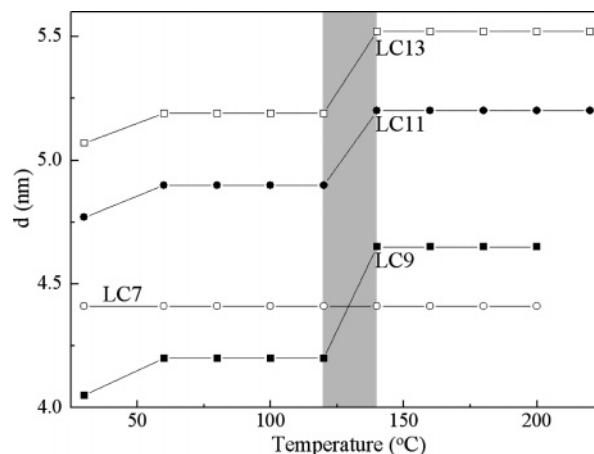

Figure 7. Change of long period spacing determined by the primary peak of the X-ray scattering results. Data points of LC13 (□), LC11 (●), LC9 (○), and LC7 (■) are based on the *d*-spacing values from X-ray scattering at various temperatures, respectively. The dark zone corresponds to the phase transition between the SmA and SmC* phases.

Figure 6. X-ray scattering experiments of LC11 at different temperatures through cooling.

scattering experiments according to an expression $\lambda = 2d^* \sin \theta$. From chain conformation consideration, the extended chain length of LC11 (*l*) is estimated as ca. 2.84 nm so that a smectic-like bilayer structure is proposed by assuming the alkoxyl groups are nearly parallel packed between layers at which *d* = 2*l* is roughly equal to the determined *d*-spacing. Furthermore, the layer-to-layer *d*-spacing increases with the enhancement of alkoxyl chain length (Figure 7), consistent with the assumption of bilayered texture. In contrast to the

low-2θ-angle region, there is no significant diffraction identified at high-2θ-angle region in such high temperature, indicating the lack of molecular packing ordering due to the formed SmA phase.

For the intermediate transition, the layer-to-layer *d*-spacing appears to be 4.90 nm. We speculate that the reason for *d*-spacing variation from the highest transition is attributed to the director (i.e., molecular chain) tilting and the director is tilted ca. 20° away from layer normal on the basis of the proposed SmC* in previous section. With further annealing or cooling, crystallization may occur from the pre-existent SmC* phase so that high ordered phase with lateral packing order can then be formed at which reflections in the high-2θ-angle region in the X-ray profile such as the broad reflection at 2θ of 19.1° can be found. Consequently, the ordered lateral packing is determined as *a* = 1.80 nm and *b* = 0.46 nm according to the reflections of (200) (2θ of 9.8°) and (220) (2θ of 19.1°). Upon cooling below the glass transition temperature (i.e., the lowest transition), the layer spacing slightly changes to 4.77 nm and the director is tilted ca. 23° away from the layer normal. The SAED method is then applied to further examine the structural packing information on thin-film samples. Figure 8 shows the SAED pattern from the highly crystalline region (Figure S3 of Supporting Information) at which [00*l*] zone diffraction can be obtained so that ordered lateral packing is determined as *a* = 1.80 nm and *b* = 0.47 nm, very consistent with the
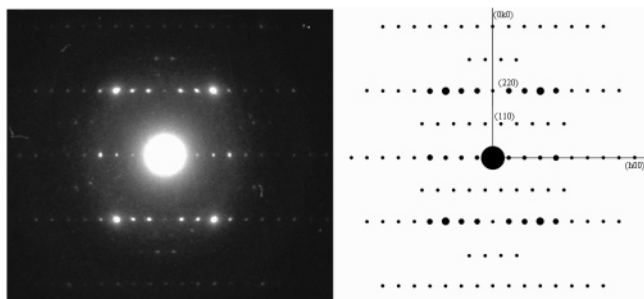
Figure 8. SAED pattern for isotropic melt-crystallized LC11 taken from high-crystalline region along the [00*l*] zone.

Figure 9. High-resolution TEM image of LC11 crystallized at 125 °C from the isotropic melt and then gradually cooled to ambient temperature.

dimensions determined from X-ray results. Moreover, high-resolution TEM image shows the ordered lamellar morphology in Figure 9. The ordered lamellar structure gives ∼4 nm crystalline spacing and the dark region corresponds to the Schiff-based rod segment whereas the light region corresponds to the glass state region of alkoxyl chains, suggesting the formation of a bilayer structure. Similar results can also be obtained for the chiral Schiff-based rod−coil amphiphiles in this study besides LC7 (Figure 7). No significant change on the layer-to-layer *d*-spacing in LC7 can be found, indicating the absence of phase transformation from SmA to SmC*.

According to the morphological observations and X-ray scattering studies, we suggest that the formation of the SmC* liquid-crystalline phase may be strongly associated with the execution of isothermal crystallization in the intermediate temperature region of the chiral Schiff-based rod−coil amphiphiles. To simply explain the specific phase behavior, G-T relations having an enantiotropic-type liquid-crystal system were proposed (Figure 10). Starting from isotropic phase, the change on slope (i.e., entropy concern) is attributed to the formed corresponding LC phase upon cooling. The intersecting point of the lines presents the phase transition temperature. The phase transition temperature can be determined via DSC profiles. When the temperature continuously decreases from the highest temperature region, the formation of the kinetic controlled phase, in particular, the SmC*, is strongly dependent upon the cooling rate so that the SmA
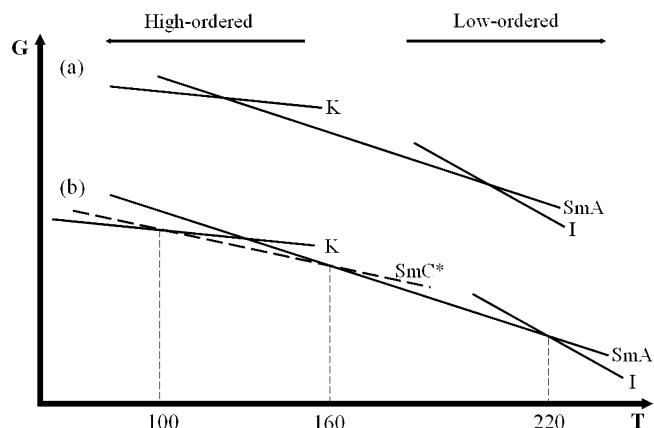

Figure 10. Tentative G-T diagram for (a) LC7 and (b) LC11. The SmC* will not be present in LC7.

phase remains under fast cooling due to the least time to achieve phase transformation. By contrast, the transition response from SmA to SmC* may be identified by DSC thermograms in the slow cooling process as shown in Figure 1. Interestingly, this phase transition cannot be found in the samples with shorter alkoxyl chain length such as LC7. It is noted that no banded texture can be found in LC7. As a result, we speculate that the appearance of the banded texture is attributed to the occurrence of a crystallization process originating from the liquid-crystalline phase with helical sense, namely, SmC* phase.

On the basis of the morphological observations and structural analyses, the phase transition sequence from high temperature to room temperature is found as I → SmA → SmC* → K → T_g for the chiral Schiff-based rod−coil amphiphiles with longer alkoxyl chain length. By contrast, the phase transition of SmA → SmC* is absent while the alkoxyl chain length is shorter than a critical value (for instance, LC7), leading the phase transition sequence of I → SmA → K.

Self-assembled Hierarchical Superstructures. The formation of unique banded texture leads to the following question: how the evolution of self-assembled chiral Schiff-based rod−coil amphiphiles performs from molecular level to self-assembled morphology in different length scales, in particular, from point chirality to supramolecular chirality, finally chiral phase. The morphologies of hierarchical superstructures were obtained by solution casting the samples on carbon-coated substrates to form thin films, and then self-assembly through specific thermal treatments was carried out as described in the Experimental Section. Figures 11a−11d exhibit the morphological transformation of hierarchical superstructures from platelet-like texture to the left-handed helical morphology as observed by TEM. As shown, the LC7 shows a platelet-like morphology (Figure 11a). By contrast, obvious helical twists (say in Figure 11c of LC11) can be found once the alkoxyl chain length reaches a large enough size. In LC9 (Figure 11b), the self-assembled textures present mixed morphologies, including platelet-like morphology and helical morphology, suggesting the behavior of transitional composition for the self-assembled morphologies. The morphology of LC13 (Figure 11d) is also identified as left-handed helical morphological texture. The effect of alkoxyl
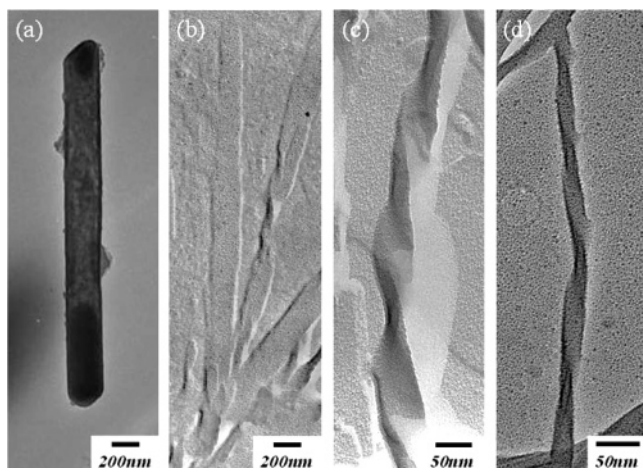
Figure 11. TEM images of hierarchical superstructures in which samples crystallized at 125 °C from the isotropic melt and then gradually cooled to ambient temperature: (a) LC7, (b) LC9, (c) LC11, and (d) LC13.

chain length on the self-assembled superstructure in bulk (i.e., thermotropic LC type) is similar to that in solution (i.e., lyotropic LC type) as found in our previous study.[28] Consistent with theoretical predictions, the size of adjacent alkoxyl chain length determines the threshold of twisting for the formation of helical morphology. It is also noted that the pitch length of the helical twists (that is inversed twisting power) decreases with the enhancement of alkoxyl chain length. Most importantly, the induction of helical super-structure attributed to the occurrence of critical twisting power (namely, the significant chirality effect) corresponds well with the observation of banded spherulites. It is intuitive to suggest that the formation of banded spherulites is strongly dependent upon the chiral transformation from molecular level to hierarchical superstructure, finally the morphological textures in macroscopic bulk (see below for details).

Origins of Banded Spherulites in Liquid Crystals. In contrast to the normal spherulites for crystalline LC7, banded spherulites in the chiral Schiff-based rod−coil amphiphiles with higher alkoxyl chain length, such as LC9, LC11, and LC13, can be distinctly observed by PLM. Consequently, hierarchical superstructures with helical sense for the self-assembly of the chiral amphilphiles can be found once the alkoxyl chain length reaches large enough size. Consistent with the observation of helical superstructures, the occurrence of SmC* phase can only be found in samples with enough alkoxyl chain length. The coincidence with respect to the alkoxyl chain length effect on self-assembled hierarchical structure (i.e., the tertiary structure) and the spherulitic morphology (i.e., the quaternary structure) suggests the existence of strong correlation for morphological evolution from the molecular level to the macroscopic object with the formation of SmC*.

Considering the bilayer molecular disposition in the self-assembled superstructure, a hypothetic model about the morphological evolution from the molecular level to hier-archical superstructure and finally to macroscopic texture is illustrated in Figure 12. As shown, the molecular chains self-assemble as parallel packing (Figure 12a) for the amphiphilic molecules as evidenced by X-ray scattering results (Figure 6) so that a smectic-like bilayer structure can be found as
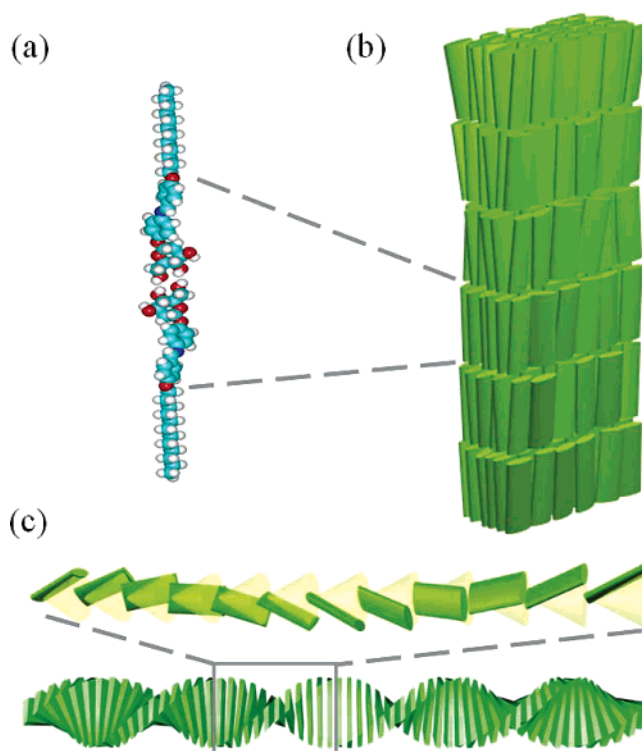

Figure 12. Schematic illustration of LC11 for different LC phases in the self-assembly: (a) Secondary structure via parallel molecular packing; (b) SmA phase; (c) SmC* phase. The gray line indicates the SmC* phase along the single-crystal axis with helix sense.

evidenced by TEM (Figure 9). At high temperature, the SmA phase with homeotropic anchoring condition with respect to the glass substrate is formed as illustrated in Figure 12b, resulting in a transparent PLM image. Annealing the samples at lower temperature (for instance, 125 °C in LC11) leads to the formation of the SmC* phase from SmA in samples with enough alkoxyl chain length. Consequently, the layer-to-layer *d*-spacing decreases during the transition from the SmA to SmC* phase (for instance, from 200 to 125 °C) as shown in Figure 7 at which the tilting of the molecular director can be efficiently achieved by isothermal crystal-lization process. The morphological evolution from second-ary to tertiary helical superstructure is illustrated in Figure 12c. As shown, the tertiary superstructure with helical sense (Figure 11) of the chiral Schiff-based rod−coil amphiphiles, which is a smectic-like bilayer structure with the parallel packed alkoxyl groups between layers, is the self-assembly result of SmC* phase. Consistent with the theoretical models with respect to the chiral transfer from point chirality to supramolecular chirality in the literature,[22−27,36] the bending curvature of the self-assembly chiral amphiphiles is induced by the chiral sugars so that significant bending could be achieved by introducing longer enough alkoxyl chain length. Banded spherulites are identified as quaternary chiral struc-ture, which are regarded as a collection of tertiary chiral structures with SmC* phase (i.e., helical twists). Note that the size of adjacent alkoxyl chain length determines the threshold of twisting for helical formation through primary

(36) Aggeli, A.; Nyrkova, I. A.; Bell, M.; Harding, R.; Carrick, L.; Mcleish, T. C. B.; Semenov, A. N.; Boden, N. *Proc. Natl. Acad. Sci. U.S.A.* **2001**, *98*, 11857−11862.
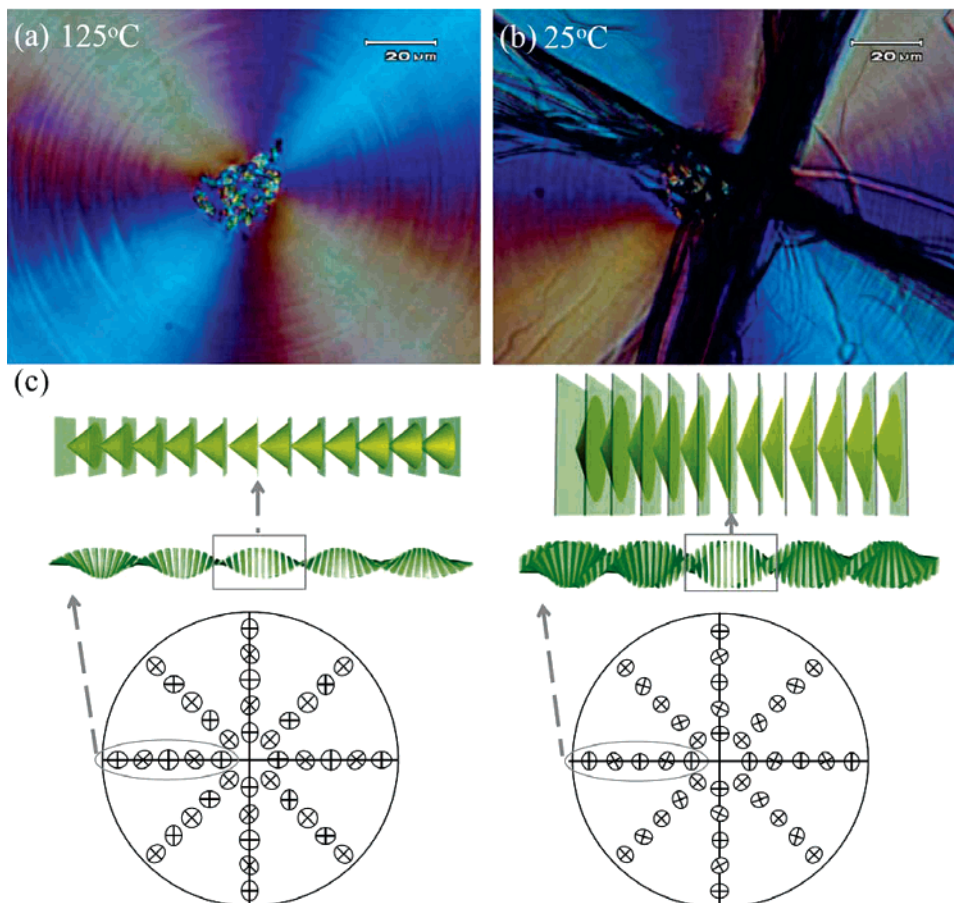
Figure 13. PLM images of LC11 (a) at 125 °C (positive-birefringence spherulite) and (b) at 25 °C (negative-birefringence spherulite). (c) Indicatrix rotation of SmC* phase along the helix axis and the *d*-spacing change affect by temperature.

structure to quaternary structure. As a result, the phase transition of SmA → SmC* is absent in LC7 due to the low helical twisting power of LC7. As a result, the formation of banded spherulites is attributed to helical strands along the spherulitic radials. Several single helical strands would grow from the center that gives regular extinction when the optical axis coincides with the polarization plane in PLM. Figure 13a shows the positive birefringence at 125 °C, indicating that the molecular director is approximately parallel to helical axis. However, the banded extinction is unable to be clearly explained in terms of simple uniaxial indicatrix on the basis of SmC* consideration. We thus suggest that the occurrence of zero birefringence behavior is mainly attributed to the specific primary structure (i.e., sugar-based structure) of the chiral Schiff-based rod−coil amphiphiles. So the difference in refractive indices along the meridian and latitude directions of the sugar-based structure should be significant, resulting in the optical anisotropy with the refractive index $n_c > n_a > n_b$ instead of $n_c > n_b \sim n_c$ for the chiral Schiff-based rod−coil amphiphiles (Figure 14a).[37] Upon twisting and bending, the refractive index $\mathbf{n_c}^*$ (i.e., the project dimension of the n_c principal axis) may be almost equal to the n_b as shown in Figure 14b. Banded extinction thus takes place when the direction of rotative optical axis leads into $n_b = n_c^*$ in PLM (i.e., zero birefringence of the SmC* phase in Figure 14c).
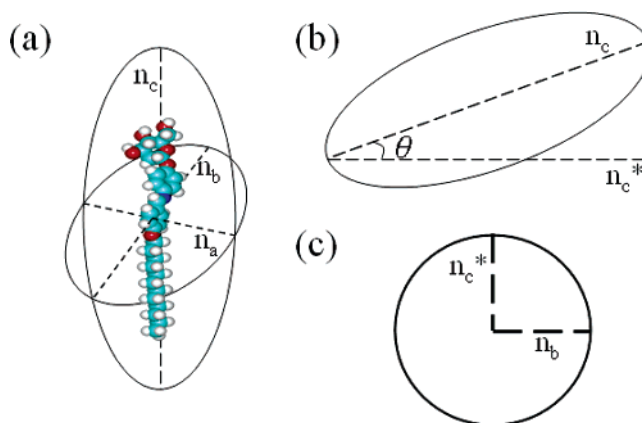

Figure 14. (a) Diagram of a biaxial indicatrix (refractive index ellipsoid), showing the refractive index $n_a > n_b > n_c$ of chiral Schiff-based rod−coil amphiphiles. (b) Biaxial indicatrix tilt makes the decrease of n_c to n_c^*. (c) Intersection of the indicatrix and of the wave plane. Zero birefringence of indicatrix rotation produces dark line of banded spherulites in PLM.

Moreover, interesting morphological transformation from positive to negative birefringence under PLM was observed, further confirming the formation of banded texture resulting from sugar moiety induced SmC* phase as shown in Figure 13b. Upon temperature variation, the molecular director gradually tilts away from layer normal of SmC* phase so as to achieve birefringence change from positive to negative during cooling. Figure 13b shows the negative birefringence at 25 °C that the molecular director is approximately normal to the helical axis. Also, upon the changes on the molecular

(37) Samir, M. A. S. A.; Alloin, F.; Dufresne, A. *Biomacromolecules* **2005**, 6, 612−626.

director, the SmC* bilayer structure shrinks, thus causing a fractured morphology (Figure S4 of Supporting Information).

Present works show that the twisted superstructure and banded shperulites (i.e., SmC* phase) are due to the chiral effect in the self-assembly of chiral Schiff-based rod−coil amphiphiles. Consequently, the formation of banded spherulites is induced by chirality effect from a molecular level. The self-assembled morphology of platelet-like and helical twists morphology is tuned by the relative alkoxyl chain length. We thus suggest that chain tilting of the molecules within the bilayer attributed to the chirality of the constituents provide a natural explanation for the observed helical morphology so as to correlate with the observed SmC* phase. The experimental observations here may give the prospect of helical morphologies in different length scales of amphiphilic bilayer systems.

Conclusion

A series of chiral Schiff-based rod−coil amphiphiles have been systematically synthesized to examine the chiral effect on the self-assembly of supramolecules. As revealed, the self-assembly of the chiral amphiphiles provide a simplified system to explain the chirality transfer from the molecular level to macroscopic size. A unique texture of banded texture can be obtained and identified as macroscopic chirality that is composed of several helical twists. Eventually, the helical twists are formed by the self-assembly of the bilayer characteristic having parallel packed alkoxyl groups as well as the well-packed sugar entities. We aspire to establish a universal behavior of the chiral effect on the self-assembly in simple design.

Supporting Information Available: The crystal and typical ordered LC texture determinations for the series of chiral Schiff-based rod−coil amphiphiles (PDF). This material is available free of charge via the Internet at http://pubs.acs.org.

CM061666G